Vacuum 207 (2023) 111686

Contents lists available at ScienceDirect

Vacuum

journal homepage: www.elsevier.com/locate/vacuum

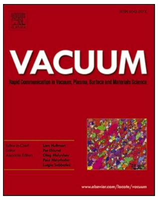

Electron-beam chemistry in graphene - Effect of environmental SEM parameters on patterning and defect engineering

Ryan Selhorst [a,b], Michael A. Susner [a], Ryan Muzzio [c], I-Hsuan Kao [c], Jennifer Carpena-Núñez [a,b], Ahmad E. Islam [a], Jyoti Katoch [c], Benji Maruyama [a], Rahul Rao [a,*]

[a] Air Force Research Laboratory, Wright-Patterson AFB, OH, 45433, USA
[b] UES Inc., Dayton, OH, 45432, USA
[c] Department of Physics, Carnegie Mellon University, Pittsburgh, PA, 15213, USA

ABSTRACT

The engineering of defects in low-dimensional materials can enable the modulation of their optical, electrical, thermal, and structural properties. We have previously shown the ability to engineer precision patterned defects in graphene by electron beam irradiation in a controlled water vapor ambient within an environmental scanning electron microscope (ESEM). However, the relationship between instrumental parameters and structural changes in graphene are unexplored. Here, we investigate the relationships between parameters such as pressure, electron dose, and acceleration voltage on the electronic and structural properties of graphene as probed by Raman spectroscopy. There are dependencies on all of the studied parameters but electron dose is the dominant parameter that shows the most intense levels of structural modulation. Interestingly, control of instrumental parameters allows for the precision tailoring of features such as resolution (as determined by the beamskirting effect), doping, and functionalization – all of which make this process powerful for precision tuning of 2D materials and adds an enhanced technique for the development of next-generation electronics.

1. Introduction

Lattice defects are ubiquitous in two-dimensional materials (graphene and related two-dimensional materials) and play a significant role in their electronic, optoelectronic, thermal, surface, and structural properties of [1–6]. These defects are present in many form such as vacancies, dislocations, grain boundaries, dopants, and adsorbates, and must be minimized for achieving the best electrical, thermal, and structural properties. Conversely, lattice defects can be beneficial for controlling hole/electron doping, optoelectronic and sensing properties, as well as surface reactions. Over the past decade, several methods have been demonstrated for the introduction of defects in two-dimensional materials; however, these methods do not offer precision control and thus can readily cause adverse effects. For example, polymer-based lithography, which is traditionally used to pattern graphene has been found to significantly reduce its device performance [7–9]. Solutions to mitigate this include grain boundary engineering to control field-effect mobility [10] and van der Waals encapsulation by hexagonal boron nitride [9]. However, in all of these cases, lithographic techniques limit the feature sizes to ~10 nm due to the use of photoresists and limits imposed by the energy of the electromagnetic radiation.

Higher resolution can be achieved by using electron beams (e-beams), and previous uses of e-beam for defect engineering in graphene involved a high acceleration voltage (80–300 kV) inside a transmission electron microscope [11] to control the elastic (e.g. atomic displacement, knock-on damage) and inelastic (*e.g.* heating) mechanisms induced by the e-beam. These high energy e-beam processes etched carbon atoms from the graphene lattice [11–17], rotated bonds in the lattice [12,18], and manipulated foreign atoms introduced during graphene processing [13,14,17]. Other processes either used a lower acceleration voltage (5–20 kV) to remove pre-existing defects (*e.g.* hydrogen [19] and fluorine [20]) from graphene or defined nanostructures in graphene (or carbon nanotubes) through etching C atoms away [21–25]. E-beam exposure experiments inside a scanning electron microscope (SEM) have revealed a dose-dependent modulation of the carrier density in graphene, attributed to charges generated at the interface with the substrate (typically SiO_2) [26–30]. Importantly, all of these processes use the e-beam to manipulate atoms that are *already present* within the graphene lattice or on its surface without any controlled chemistry through substitution reactions.

We have previously reported a mask-less, resist-free, and reversible process for engineering functionalities in chemical vapor deposition (CVD)-grown graphene at a present resolution of ~60 nm with values < 10 nm within reach [31,32]. Our process involves e-beam chemistry and

---

* Corresponding author.
E-mail address: rahul.rao.2@us.af.mil (R. Rao).

https://doi.org/10.1016/j.vacuum.2022.111686
Received 28 August 2022; Accepted 15 November 2022
Available online 21 November 2022
0042-207X/Published by Elsevier Ltd.

is depicted schematically in Fig. 1a. The experiments are performed inside an environmental SEM (ESEM) in the presence of a controlled environment such as water vapor. First, highly energetic radical species are produced by radiolysis inside the ESEM through interaction of the gas species with the e-beam and with secondary electrons generated from the irradiated volume. The interaction area of the short-lived radiolysis products (in our case, those derived from H_2O [33–35]) with the graphene surface is defined by the interaction volume of the e-beam. This volume depends on its elemental composition of the specimen (including any underlying substrate), the electro-optical configuration, and the acceleration voltage. With the e-beam focused on the graphene surface, radiolysis products generated in the vicinity of the irradiated area can react with the carbon atoms in the graphene lattice and hence modify or remove the atoms, thereby creating defects or adding functional groups to the graphene.

As the reaction surface area is influenced by the interaction volume, one can potentially engineer functionalities at a specific atomic location with a high resolution e-beam. Alternately, one can create complex patterns by rastering a broader e-beam across a substrate-supported sample, as illustrated in Fig. 1b, which depicts an SEM image of a graphene surface patterned with the emblem of the United States Air Force (USAF). The outline of the emblem can be discerned in Fig. 1b due to a controlled amount of adventitious carbon deposited onto the surface. The corresponding Raman intensity map in Fig. 1c shows a much more striking contrast where the defect density in the pattern is plotted as the ratio of intensities (I_D/I_G) of the disorder-induced D peak ~1350 cm^{-1} (with the 514.4 nm excitation wavelength) and the sp [2] carbon stretching mode ~1580 cm^{-1}. The D peak in graphene arises from intervalley scattering of a transverse optical (TO) phonon with a lattice defect [36–38], and the I_D/I_G value has been extensively used as a qualitative measure of the defect density in sp [2] carbon materials (graphite, graphene and carbon nanotubes) [37,39–41]. X-ray photoelectron spectroscopy (XPS) analysis on our patterned graphene revealed the origin of the defects to be functionalization of the graphene surface with hydroxyl (C–OH), epoxide (C–O–C) and carboxyl (-COOH) groups and computational modeling showed that electron transport within the nanoscale patterned region was comparable to that in graphene nanoribbons [31,42]. Individual Raman spectra from the graphene outside and inside the patterned area are displayed in Fig. 1c, and show the D and G peaks in addition to the second order 2D peak, which arises from the scattering of two TO phonons from the *K* point of the graphene Brillouin zone. In addition to these peaks, a second disorder-related peak, labeled D′ can be observed in the spectrum from the patterned region. The D' peak arises from intravalley scattering of a TO phonon with a lattice defect, and its intensity has been shown to be sensitive to the type of defect in the graphene lattice, i.e. sp [3] or vacancies [43].

Having demonstrated that e-beam chemistry can be used to pattern and functionalize graphene, we next show how the various processing parameters in the ESEM can be used to tune and optimize the resulting patterns. Since Raman spectra from graphene offer insights into its physical properties, our primary metrics of interest are the Raman spectral features, namely the frequencies and widths of the D, G, D' and 2D peaks, as well as the I_D/I_G ratio as a measure of the functionalization (or defect density) in graphene. Among the many interrelated process parameters in the ESEM, the physics of the e-beam is nicely captured by the total beam dose (in units of $\mu C/cm^2$), which is given by the relationship Dose $= (t_d)(I_{beam})/\Pi$ [2]. Here Π is the shot pitch (*i.e.* the spacing between e-beam probe positions), t_d is the dwell time, and I_{beam} is the beam current. Therefore, the variables under investigation for pattern optimization are 1) pressure, 2) voltage, 3) dwell time, 4) pitch, and 5) beam dose. In this study, we systematically probed each of these variables in a parametric study by varying each variable and keeping the others constant in order to see their effects on the Raman spectral features of graphene. Our study not only identified the optimal parameters for controlling the defect density (and thereby functionalization) in graphene, but also reveals the fundamental physics of the e-beam chemistry process.

2. Experimental

2.1. Graphene synthesis by chemical vapor deposition

Graphene was grown on Cu foil using low-pressure chemical vapor deposition and then transferred using polymethylmethacrylate (molecular weight ~ 950 K; dissolved 1% w/v in anisole) onto a Si substrate

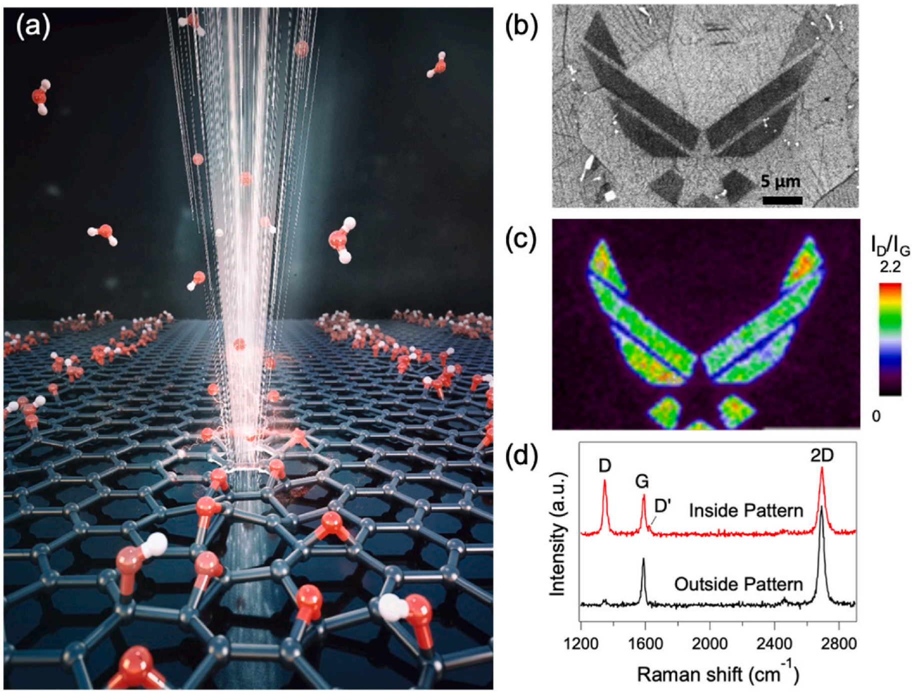

Fig. 1. E-beam chemistry in graphene. (a) Schematic of the e-beam process for patterning and functionalization in graphene. (b) SEM image showing the U.S. Air Force emblem patterned into graphene. The contrast in the SEM image comes from adventitious carbon deposited on to the patterned region. (c) Corresponding Raman intensity map showing the defect density (I_D/I_G ratio) in the patterned region. (d) Raman spectra from two spots inside and outside the patterned region in (b). The defect-related D and D′ peak intensities are highest inside the pattern and barely measureable outside of it.

with a ~285 nm thick SiO_2 layer as described in an earlier work [31]. The graphene-coated Si/SiO_2 substrates were then subjected to the following radiolysis procedure.

2.2. *Mechanical exfoliation of graphene*

Si/SiO_2 (300 nm oxide thickness) substrates (University Wafers) were diced and cleaned by sonication in acetone and then IPA separately. Then graphite (2D Semiconductors) was placed on an adhesive plastic film (blue tape) from Ultron Systems (P.N. 1009R-6.0). We chose the least sticky tape to reduce the amount of tape residue produced on the substrate. By taking a second blue tape, we propagated the bulk graphite across the tapes until they were densely packed with graphite. We targeted regions of the tape that had graphite planes protruding perpendicular to the tape's plane and placed the substrate SiO_2 face on the tape. Flipping the tape over, we rubbed the tape with carbon-tipped tweezers such that the tweezer was in contact with the tape/SiO_2 interface. The final step was to release the tape while keeping the tension at a maximum by holding the substrates as we remove the tape.

2.3. *E-beam chemistry experiments*

E-beam chemistry and SEM imaging were performed using a Zeiss Gemini system. Using a 15 μm condenser aperture which begets a 1.6 nm probe size. To obtain control of the pressure range in the Zeiss Gemini system, we used the variable pressure (Nano-VP) mode which placed a pressure-limiting aperture (called a beam-sleeve) in the path between the e-beam column and the vacuum chamber; the 350 μm aperture was used in order to reduce skirting effects. All patterning in the Zeiss Gemini SEM was performed in conjunction with a beam blanker (Raith Nanofabrication; HVP 8000) controlled via the Nanometer Pattern Generation System (NPGS v.9.1).

2.4. *Raman spectroscopy and analysis*

Raman spectra were collected with a Renishaw inVia confocal Raman microscope. Typical excitation laser ($\lambda = 514.5$ nm) power was ~1 mW with a ~0.7 μm spot size; 1800/mm gratings were used. During spectral acquisition, the characteristic Si vibrational mode at ~520 cm^{-1} was used for calibration. Analysis of Raman spectra was performed using the following routine in MATLAB: 1) background subtraction was performed using a linear approximation, 2) fitting of the 1050 cm^{-1} to 1750 cm^{-1} region of the spectra using five Raman bands (three of these bands, i.e. D-, G- and D'-bands for graphene, have standard peak positions and widths), and 3) we fit the 2600 cm^{-1} to 2800 cm^{-1} region of the spectra using a single Raman band corresponding to the 2D-band for graphene. This fitting enabled estimation of the I_D/I_G, I_{2D}/I_G, $I_D/I_{D'}$, ω_D, Γ_D, ω_G, Γ_G, $\omega_{D'}$, Γ_D, ω_{2D}, and Γ_{2D} parameters.

3. Results and discussion

3.1. *Effects of pressure and dwell time on defect density*

The first experimental parameter investigated was the water vapor pressure within the ESEM chamber. A series of patterning experiments were performed at pressures from 5 to 30 Pa and I_D/I_G values were measured for each experiment. These experiments were performed at doses ranging from 275 to 2750 $\mu C/cm^2$ for three values of Π: 9.96 nm, 15.39 nm, and 19.92 nm. Values of t_d were varied slightly between 40, 60, 80, and 100 μs to keep doses the same among the various pressure experiments as the beam current decreased with increasing pressure due to increased scattering. As is evident from the graphs in Fig. 2a-c, the defect densities exhibit a parabolic trend with increasing pressure, with a maximum around 20 Pa. This trend is the same for all the shot pitch (Π = 9.96, 15.39 and 19.92 μm) and dwell time (t_d = ~40, 60, 80 and 100 μs) values studied. This likely represents two competing phenomena: 1) at low pressures, there is a dearth of species available to create radiolysis products for e-beam chemistry; 2) at higher pressures, the beam is

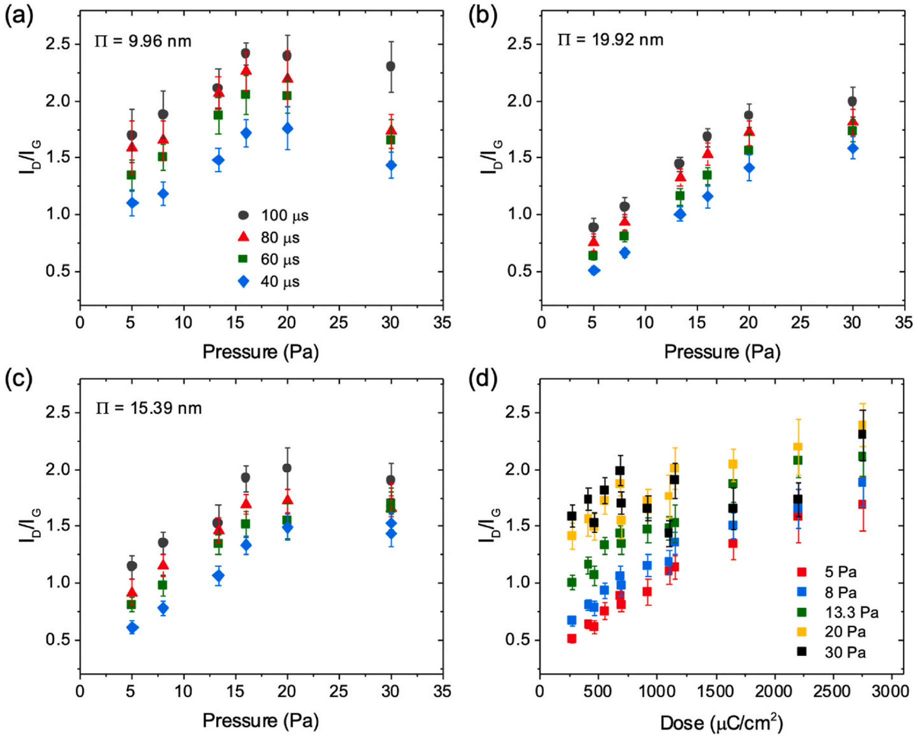

Fig. 2. Effect of water vapor pressure on defect density in graphene. (a)-(c) I_D/I_G values as a function of pressure for varying dwell time (t_d) and pitch (Π) values. For a given pitch and dwell time, the defect densities can be tuned by up to a factor of 3. (d) The same data as in (a)-(c) replotted as a function of electron dose.

attenuated by the excess of radiolysis species present in the chamber. When the data is replotted in terms of dose (Fig. 2d) we see that, for a given pressure, only dose matters with respect to the level of defect density in the patterned area up through pressures of 20 Pa. At higher pressures and doses, there is a marked reduction in the defect densities, with a non-monotonic dependence on the electron dose, which we attribute to perturbations and gas currents within the chamber.

The pressure-dependence study was also useful to determine the optimal parameters for functionalization such that adjacent graphene remains unaltered. A metric that can be used for this is to compare the I_D/I_G of the intentionally patterned area [$(I_D/I_G)_{pattern}$] to that of the I_D/I_G of an adjacent area [$(I_D/I_G)_{skirt}$] that is intended to remain in a pristine state. This is related to a well-known effect called beamskirting where the scattering of the e-beam with the gaseous species inside the ESEM can cause a reduction of the beam current within the focused area and its redistribution to form a “skirt” around that area [44]. The metric $(I_D/I_G)_{pattern}/(I_D/I_G)_{skirt}$ is therefore ideal at ∞. In Fig. 3a we plot this metric as a function of pressure. We note that, with the exception of the 30 Pa value (which we noted in Fig. 2 had instabilities associated with its dose dependence), lower pressures lead to better patterning in terms of prevention of the beamskirt effect and unintentional modification of graphene outside the patterned area. Overall, $(I_D/I_G)_{pattern}/(I_D/I_G)_{skirt}$ improved from $\sim$1.5 to $\sim$4 just by lowering the pressure to 5 Pa (the minimum allowed by our instrument in variable pressure mode).

Next, we investigated the effect of dwell time on the beamskirt effect, at constant pressure (5 Pa, as determined from our analysis shown in Fig. 3a), electron dose (2680 μC/cm^2) and acceleration voltage (2 kV). The results are shown in Fig. 3b. From this chart we see that $(I_D/I_G)_{pattern}/(I_D/I_G)_{skirt}$ can be as high as 15 at the lowest dwell time of 0.4 μs. As mentioned above, the total dose is proportional to the dwell time but is inversely proportional to the square of Π. Therefore, to maintain the dose needed for a certain level of surface modification while reducing unintentional patterning of an adjacent region by reducing the t_d only requires a slight decrease in Π. We are, in fact, limited by our patterning software as to the minimum value of Π, which is magnification-dependent and reflects the limits of control for those conditions. The pattern of the USAF emblem shown in Fig. 1b and c were created using a t_d of 0.4 μs and a Π of 0.52 nm, the limit at this magnification. One can immediately discern that the patterning is sharp and that, through optimization of our control parameters, we were able to precisely pattern in the intended area and prevent patterning in areas that were to remain pristine. Because these conditions required high magnification, large-area patterns will require multiple iterations.

3.2. *Effects of dose and beam energy*

Next, we carefully studied the effects of beam energy and dose on the e-beam chemistry process. Analysis of the changes in the functional form of the various Raman peaks and their ratios showed that 1) we have a high degree of control over the defect engineering process in terms of tuning the strain and doping level of the graphene layer, 2) these parameters are related to fundamental changes in the structural and electronic properties of the graphene, and 3) changing the beam energy changes the evolution of the Raman profiles with dose, strongly suggesting that we can tune the functionalization through the beam energy.

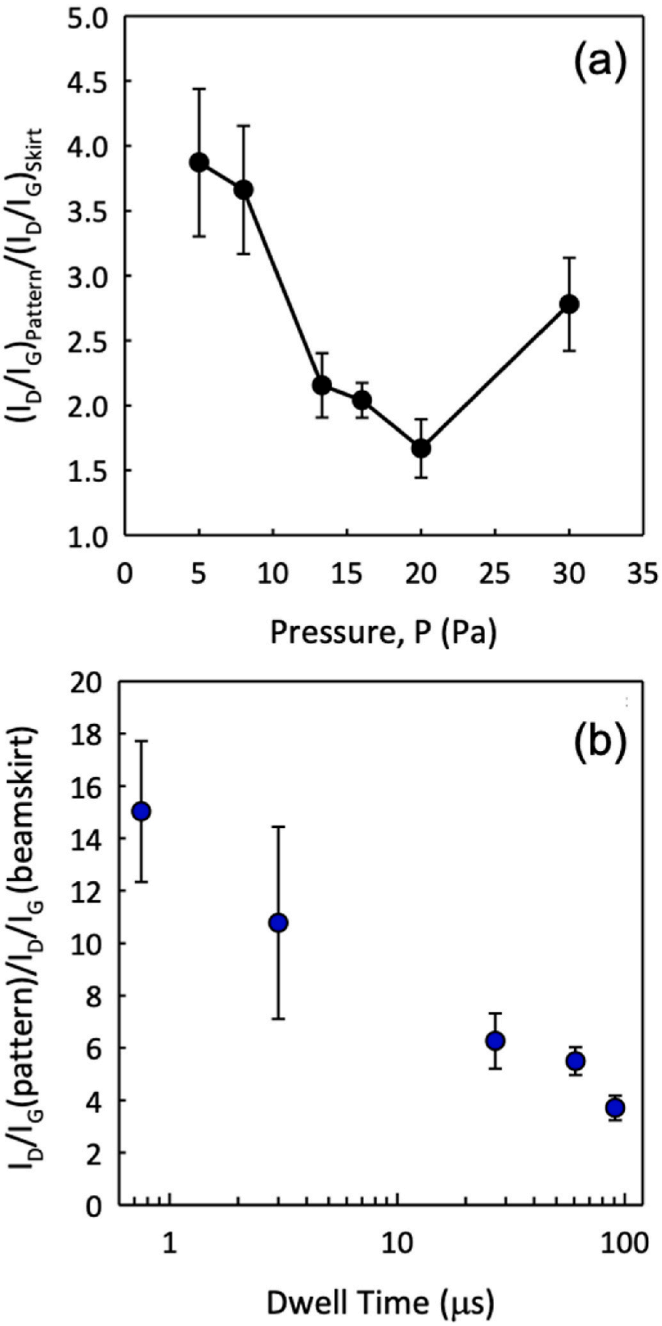

Fig. 3. Quantification of the beamskirt effect as a function of pressure and dwell time. (a) The ratio of I_D/I_G generated in the pattern over I_D/I_G generated outside of the pattern [$(I_D/I_G)_{pattern}/(I_D/I_G)_{skirt}$] as a function of pressure at a constant dose (2750 μC/cm^2), dwell time (100 μs) and acceleration voltage (2 kV). (b) $(I_D/I_G)_{pattern}/(I_D/I_G)_{skirt}$ as a function of dwell time at a constant dose (2680 μC/cm^2), pressure (5 Pa) and acceleration voltage (2 kV).The highest values of $(I_D/I_G)_{pattern}/(I_D/I_G)_{skirt}$ were obtained for the lowest pressure (5 Pa) and shortest dwell time (0.4 μs).

Fig. 4 shows the evolution of the Raman peak frequencies (ω) and peak widths (FWHM, Γ) as functions of dose for the D, G, D′, and 2D peaks of patterned graphene. These experiments were performed at a constant acceleration voltage (1 kV). Note that in order to vary the dose, we had to simultaneously vary I_{beam}, Π and t_d. From the data in Fig. 4, it is evident that increasing the dose simultaneously affected several different peak frequencies. For example, the D peak exhibited a slight but clear monotonic blueshift with increasing e-beam dose (Fig. 4a). Similarly, the G peak exhibited the same trend, though greater in magnitude (Fig. 4b). In contrast, the D′ and 2D peaks redshifted initially with increasing e-beam dosage. After an inflection point occurring between 4000 and 5000 μC/cm^2, these peak frequencies then blueshifted, with the 2D peak exhibiting the greater magnitude in shift (Fig. 4c and **d**). For peak widths Γ, all Raman peaks broadened with increasing dose, again up to an inflection point at $\sim$4000–5000 μC/cm^2. After this point, peaks either did not change in width (D and 2D, Fig. 4e and **f** respectively) or sharpened (D’ and G, Fig. 4g and **h** respectively). In graphene, the G peak typically sharpens upon doping [45] and broadens under strain [46]. The broadening (sharpening) of the G peak below (above) a critical dose therefore hints at a change in the state of

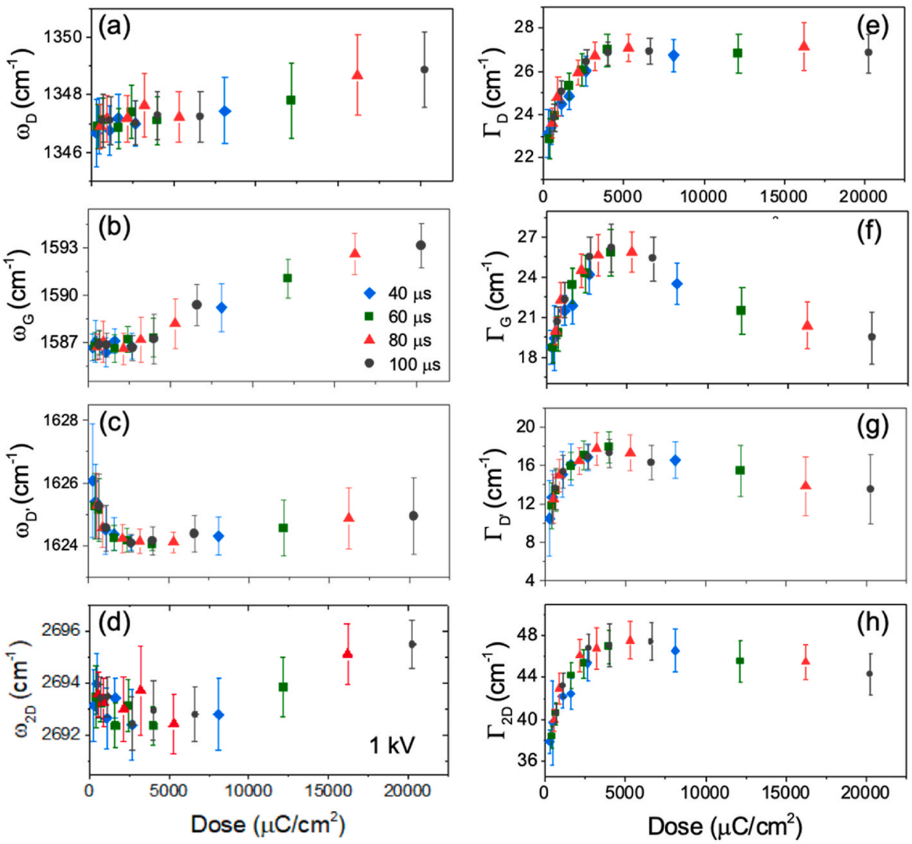

Fig. 4. Evolution of Raman peak frequencies (ω) and widths (Γ) with increasing dose. (a)-(d) Frequencies~(ω) of the D, D′, G and 2D peaks of graphene as a function of increasing electron dose. (e)-(h) Widths (FWHM, Γ) of the D, D′, G and 2D peaks of graphene as a function of increasing electron dose. The experiments were performed at 40, 60, 80, and 100 µs dwell times using an acceleration voltage of 1 kV.

the material with respect to strain and charge density. This is discussed in detail further below.

Using the relationships between the peak intensities, we can elucidate various physical properties that shed a light on the process of e-beam chemistry with radiolyzed water. In the following discussion, we address three such analyses. First, we studied the I_D/I_G ratio as a function of electron dose, at a constant acceleration voltage (1 kV) and varying dwell times (40–100 µs). Up to a certain defect concentration, the introduction of additional defects increases the probability of phonon scattering by lattice defects and thus the D peak intensity. The D peak in graphene has A_{1g} symmetry, requiring a complete 6-fold C-ring. At high defect concentrations, the probability of finding such a ring decreases and the magnitude of D diminishes. As can be determined from a plot of I_D/I_G with increasing dose (Fig. 5a), we can precisely tune the magnitude of I_D/I_G, and hence the defect spacing, simply by adjusting the dose. It is also evident from Fig. 5a that, at a fixed dose, the dwell time does not matter with respect to the measured defect density in the patterned region - t_d only plays a part in reducing or increasing the modification of the graphene surface outside of the intentionally patterned region (as shown in Fig. 3b). Interestingly, I_D/I_G increased up to a certain dose (~4500 µC/cm^2) and decreased at higher doses; this inflection point is similar to the inflection points noted for the Raman peak frequencies and widths Fig. 4. The reason for this increase and subsequent decrease in I_D/I_G is related to strain and doping in the graphene and is explained in greater detail further below.

As mentioned in the Introduction section, $I_D/I_{D'}$ serves as an indicator of the type of defect introduced in graphene [43,47]. The fact that the two defect peaks have different dependencies on symmetry and defect concentration mean that their intensity ratio (i.e. $I_D/I_{D'}$) is a convenient tool for pinpointing the type of defect present. It has been experimentally [43] and theoretically [47] shown that sp [3] type defects (*i.e.* those that do not destroy the underlying graphene lattice) result in $I_D/I_{D'}$ ratios of ~8–13 while vacancy-type defects (*i.e.* those that do destroy the graphene lattice) result in a lower ratio, ~5–7. This discernment of defect type allows us to tune defect engineering to the limits of modification of the graphene surface and beyond to the introduction of permanent, vacancy-type defects. An analysis of the data collected at the lowest beam energy (1 kV, Fig. 5b) reveals that, with increasing dose, $I_D/I_{D'}$ remained safely within the confines of the sp [3]-type defect regime. I_{2D}/I_G behaved in a similar fashion as $I_D/I_{D'}$, decreasing steadily until a dose ~4500 µC/cm^2, after which it more or less leveled off. The intensity of the 2D peak in monolayer graphene is tied to that of the D peak since both peaks arise from TO phonons. While a defect is not necessary for the appearance of the 2D peak, the probability of the two-phonon scattering process reduces with increasing defect density. In other words, the 2D peak intensity is inversely proportional to the D peak intensity and thus we expect to see opposite trends between I_D/I_G and I_{2D}/I_G, as is borne out by the data in Fig. 5a and c.

Next, we investigated the role of beam energy (i.e. acceleration voltage) on the creation of defects. For these studies the graphene was exposed to electron doses up to 10^5 µC/cm^2 in order to test the limits of our system as well as for probing the amounts of strain and doping in the graphene, as discussed further below. For the sake of convenience, we only performed high-dose studies for limited acceleration voltages since these experiments took a considerable amount of time (up to an hour for the highest dose ~10^5 µC/cm^2). The peak frequencies and widths at various beam energies (1–6 kV) exhibited similar trends as the 1 kV data shown in Fig. 4 (the evolution of peak frequencies and widths with increasing dose for all the acceleration voltages are shown in Fig. S1). Interestingly, the changes in both frequencies and widths diminished with increasing voltage, which can be seen clearly in the plot of I_D/I_G vs.

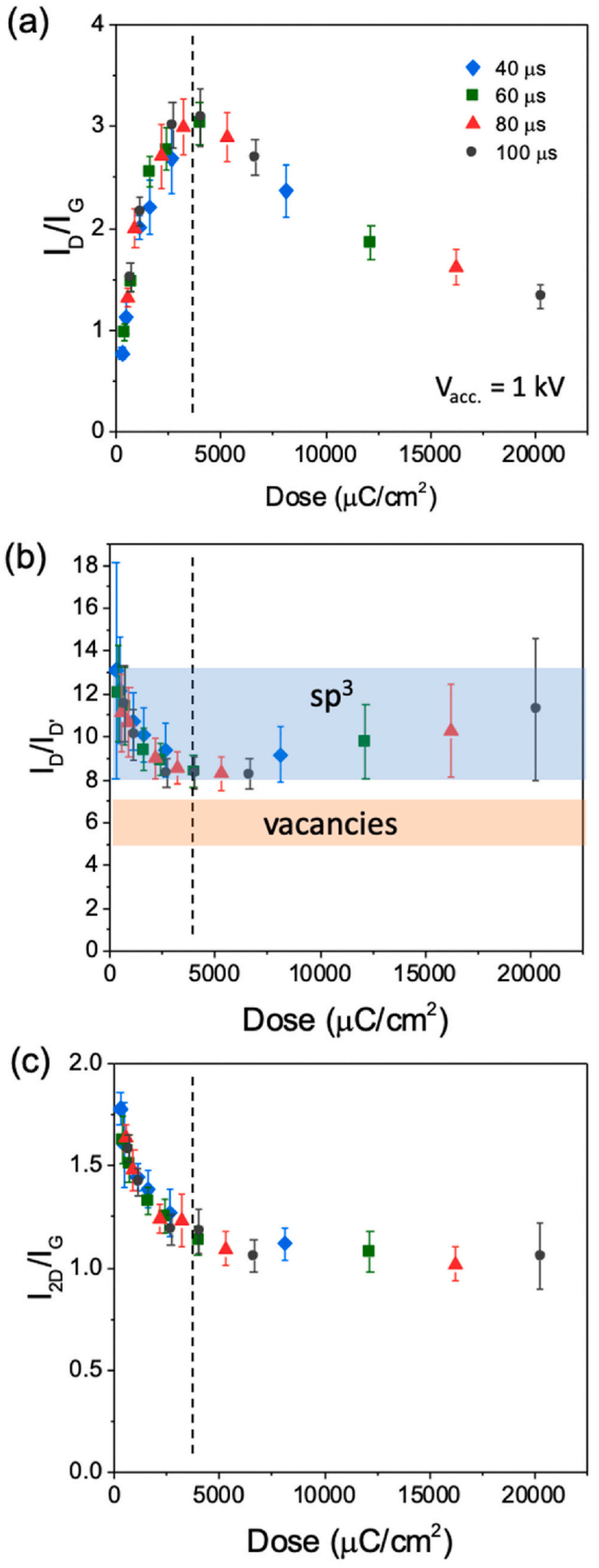

Fig. 5. Evolution of Raman peak intensity ratios with dose for varying dwell times. a), $I_D/I_{G,}$ b) $I_D/I_{D'}$ and c) I_{2D}/I_G vs. electron dose for various dwell times and at a constant acceleration voltage (1 kV).

dose in Fig. 6a. Firstly, a maximum I_D/I_G ~3 was obtained with the lowest beam energy - 1 kV. We have previously modeled epoxide functionalization in graphene and the effect of epoxide concentration on I_D/I_G, and found a theoretical maximum of ~2.5 for I_D/I_G [31]. This agrees well with the experimental data for graphene patterned with a 1 kV beam with a maximum I_D/I_G of ~3. Interestingly, this maximum value decreased monotonically with increasing beam energy while still maintaining the roughly parabolic dependence on electron dose (Fig. 6a). The I_D/I_G and I_D/I_G exhibited similar trends, with their inflection points monotonically changing with beam energy (Fig. 6b and **c**). These trends suggest that the species produced through radiolysis change with increasing beam energy. Indeed, earlier reports comparing H_2O radiolysis products produced through ^{60}Co gamma, proton, ^{4}He, ^{14}N, and ^{20}Ne ions show peroxide and H_2 formation increase with increasing radiolysis energy [48]. It is possible that similar processes are at play in the generation of radiolysis products using e-beam chemistry. The characterization of the radiolysis products and their effect on the functionalization in graphene could be performed through a combination of temperature programmed desorption and nanoscale infrared spectroscopy, something that is beyond the scope of this paper and will be the focus of a future study.

3.3. *Deconvoluting the effects of strain and doping*

As mentioned above and seen in the trends of peak frequencies with electron dose (Fig. 4), the inflection points suggest competing strain and doping effects in the graphene. These effects can be deconvoluted by plotting the G and 2D peak frequencies in a strain-doping (ε-n) plot. The G and 2D peaks have different dependencies on strain (ε) and doping (carrier concentration, n) [49,50]: Here γ is the Grüneisen parameter corresponding to the frequency of a specific peak, ω_G^0 and ω_{2D}^0 are the frequencies corresponding to zero strain for ω_G and ω_{2D}, respectively, and k_n(G) and k_n(2D) are empirical constants (-9.6×10^{13} for the G peak and -1.0×10^{13} for the 2D peak) [45]. For ω_G^0 and ω_{2D}^0, we used values obtained for suspended graphene [49,50], which can be assumed to be unstrained and undoped.

Using these relationships, we can thus generate a plot of ω_{2D} vs ω_G with superimposed strain and carrier concentration axes (Fig. 7a). Here we draw ε in increments of 0.1% and n in increments of 0.5×10^{13} cm^{-2}. Note that n in our case is the hole concentration, so we consider the graphene to be p- or hole-doped. A ε-n plot with the zero strain and doping axes along with the data corresponding to unstrained and undoped graphene (i.e. the origin of the ε-n plot) is shown in Fig. S2a. The e-beam chemistry experiments for this study were performed at a beam energy of 1 kV and water vapor pressure of 5 Pa, and the electron dose was varied from 1343 to 91000 µC/cm^2.

Fig. 7a shows the G and 2D peal frequencies of CVD graphene patterned with various doses that are color-coded from blue to red data points from minimum to maximum electron dose (1343–91000 µC/cm^2). The G and 2D peak frequencies prior to electron beam exposure (as-transferred graphene) are plotted in the ε-n plot in Fig. S2b. We note that, prior to the application of e-beam chemistry, the graphene experienced a compressive strain ~0.17% and had a hole concentration of $\sim 0.5 \times 10^{13}$ cm^2. This could be attributed to the presence of PMMA residue on the graphene surface due to the transfer process from the growth substrate (Cu foil) to the Si/SiO_2 substrate and to interactions with the Si/SiO_2 substrate. Both strain and doping are typically observed for both CVD-grown and transferred as well as exfoliated graphene on Si/SiO_2 [51–53]. Upon exposure to the lowest dose at 1343 µC/cm^2, the graphene experienced a higher compressive strain (~0.26%) and became less hole doped ($n \sim 0.2 \times 10^{13}$ cm^2). With increasing dose up to ~5000 µC/cm^2, the hole concentration remained the same but resulted in a relaxation in the strain. This is indicated by the downward arrow in Fig. 7a. At doses above the inflection point (>5000 µC/cm^2, matching the inflection points observed in Figs. 4 and 5), the strain remaining

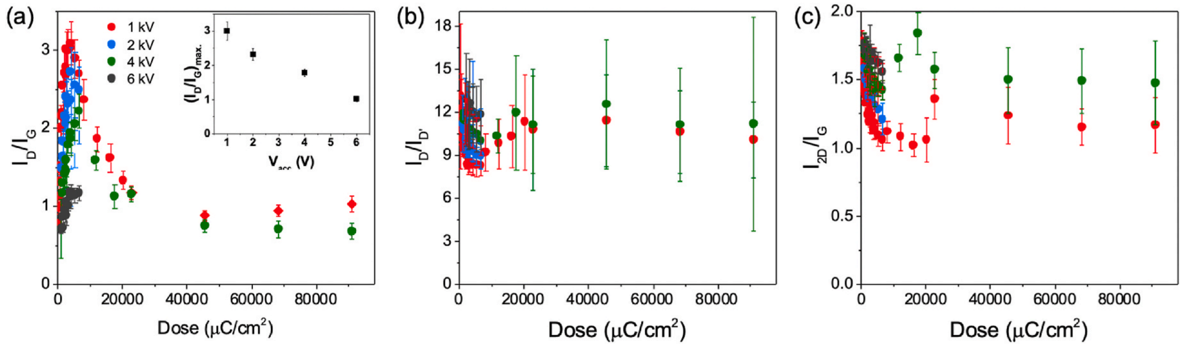

Fig. 6. Evolution of Raman peak intensity ratios with dose for varying beam energies. a), I_D/I_G, b) $I_D/I_{D'}$ and c) I_{2D}/I_G vs. electron dose for various dwell times and at a constant acceleration voltage (1 kV). The inset of a) shows the evolution of the maximum in the I_D/I_G peak as a function of voltage.

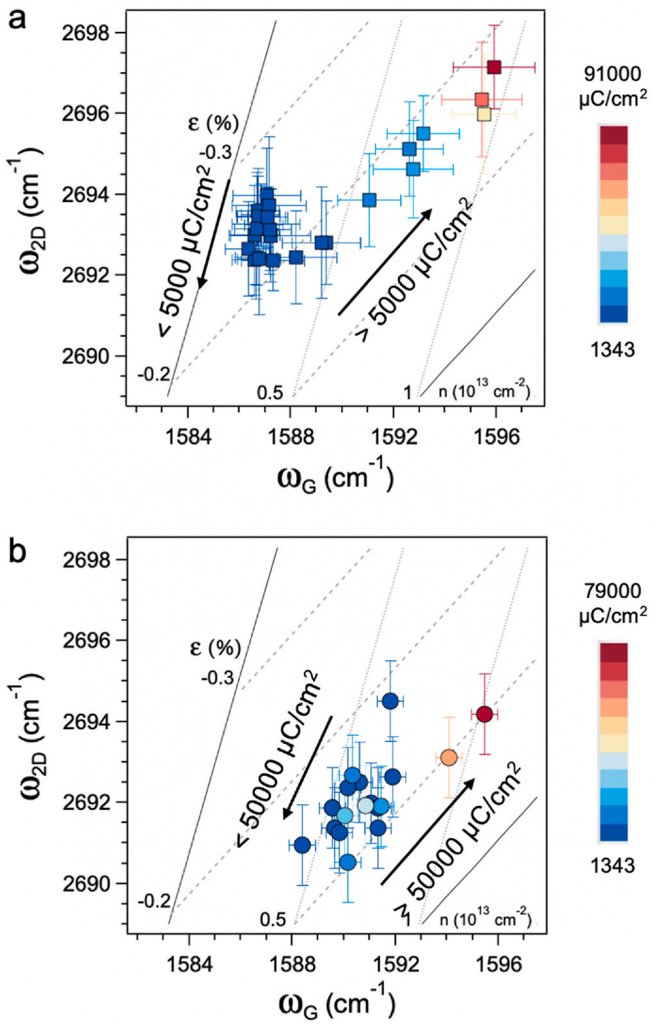

Fig. 7. Deconvolution of strain and doping in e-beam chemistry experiments performed at 1 kV in 5 Pa H_2O. *ε-n* correlation plot for a) CVD graphene, and b) mechanically exfoliated graphene. The data points in a) and b) are color-coded according to increasing electron dose from 1343 to 91000 μC/cm^2 in the case of CVD graphene, and from 1343 to 79000 μC/cm^2 for exfoliated graphene. In both cases, we see constant hole doping and tensile strain with increasing doses up to a threshold value (inflection point in the data), and increasing hole doping with constant strain at higher electron doses.

constant ~0.18% but hole concentration increased. This is indicated by the upward arrow in Fig. 7a. At the highest dose, the hole concentration reached ~1.1 × 10^{13} cm^2, over a factor of two higher than the unpatterned graphene.

In order to gain further insights into the dose-dependent strain and doping in graphene, we compared the effects of e-beam chemistry on CVD-grown graphene with mechanically exfoliated graphene, produced by the well-known “scotch-tape” method on Si substrates with the same oxide thickness as our CVD graphene samples. We conducted a series of electron dosage experiments (1343–79000 μC/cm^2) on exfoliated monolayer graphene flakes and plot the resulting G and 2D peak frequencies as a function of dose on the *ε-n* plot in Fig. 7b. The dose-dependence of the frequencies and widths of the D, G, 2D and D’ peaks are included in the Supplementary Information (Fig. S3). There are a few notable differences between the exfoliated graphene data plotted in Fig. 7b and CVD graphene (Fig. 7a) - on the whole the exfoliated graphene data were shifted towards higher (lower) G (2D) peak frequencies, suggesting lesser compressive strain and higher hole concentrations. The data also exhibited a similar inflection point where the graphene underwent tensile strain up to a threshold electron dose, and hole doping at higher doses. However, the biggest difference between the exfoliated and CVD graphene data is that the threshold dose value, *i. e.* the inflection point in the dose-dependence, was an order of magnitude higher (~50000 μC/cm^2) in the exfoliated graphene. We attribute this difference to the lower defect density in exfoliated graphene, as evident from the lower I_D/I_G values (<0.5, Fig. S3).

By comparing the *ε-n* plots in Fig. 7 with the dose-dependent intensity ratios (especially I_D/I_G) in Figs. 5 and 6, a clearer picture emerges with regards to the e-beam chemistry process in graphene. For electron doses up to ~5000 μC/cm^2 in CVD graphene, we observed a monotonic increase in I_D/I_G (Figs. 5a and 6a) along with an increase in tensile strain in the graphene lattice (Fig. 7a). Within this dosage range, the hole concentration remained the same (n ~ 0.2 × 10^{13} cm^2), implying the increase in D peak intensity is solely related to strain. We have previously shown that the incorporation of epoxide defects causes an out-of-plane displacement of ~28 p.m. for the carbon atoms bonded to the oxygen [31]. This is accompanied by a stretching of the C–C bonds around that site. The out-of-plane sp [3]-like defect and the C–C bond stretching could therefore explain the increasing D peak intensity and the strain observed with increasing dose up to ~5000 μC/cm^2. At higher doses, and with presumably increasing functionalization, we see a stronger effect of the charge depletion in graphene leading to greater hole doping.

A decrease in the D peak intensity with hole doping (and consequent reduction in Fermi level) has been observed previously and was attributed to a decrease in the number of scattering pathways for the D band due to the Pauli exclusion principle [54,55]. The same reason is also responsible for the sharpening of the G peak as seen in Fig. 4f [56], *i.e.* due to a blockage in phonon decay channels as a result of the lower electron–phonon coupling brought about by hole doping. These occur when the change in the Fermi level (ΔE_F) becomes larger than the half of phonon energy of the G peak ($\hbar\omega_G$), *i.e.* ~0.1 eV. Here $\hbar$ is the reduced Planck constant. In graphene, ΔE_F is directly linked to the carrier density with the relation $n = \left(\frac{\Delta E_F}{\hbar v_F}\right) \big/ \pi$, where v_F is the graphene Fermi velocity. Based on this relation, for a hole density of 0.2×10^{13} cm^2 (for electron doses up to ~5000 μC/cm^2, Fig. 7a) and a Fermi velocity of 1.2×10^6 m/s [57,58], the change in Fermi level is ~0.1 eV [59]. Thus, for doses beyond 5000 μC/cm^2, ΔE_F increases (Fermi level decreases due to increasing hold doping) and is accompanied by a sharpening of the G peak and lowering of the D peak intensity. The G peak intensity is largely unaffected by both electron and hole doping [59] and as a result, I_D/I_G decreases for electron doses above 5000 μC/cm^2.

It is clear from the data in Fig. 7 that the threshold doses causing the inflection points, or the transition between a strain-dominated to a doping-dominated regime, depend on the type of graphene. The fact that the threshold is an order of magnitude higher for exfoliated graphene could be ascribed to its lower overall defect density (Fig. S3). Based on the discussion above, the higher inflection point can also be attributed to the higher hole density at the inflection point (~0.4×10^{13} cm^2), and, consequently the lower Fermi level in exfoliated graphene. But the overall similarities in the dose-dependent behavior of both CVD and exfoliated graphene highlight the potential to pattern, functionalize and dope different graphene samples in a controlled manner.

Finally, we note that while all of our ESEM experiments were performed in a Zeiss Gemini SEM, some limited initial studies were also performed in a different SEM (FEI Quanta 650). These alternate experiments produced very similar results with respect to the effect of the ESEM parameters on the I_D/I_G values in graphene. However, the absolute values of the parameters varied between the two microscopes due to inherent differences in instrumentation. Nevertheless, our experiments suggest that the defect engineering in graphene can be universally conducted in any ESEM provided the pressures, voltages, dwell times, shot pitch values, and doses can be carefully quantified and/or controlled. Our claim is also supported by the previously reported observation of a peak in the I_D/I_G ratio around 5000 μC/cm^2 by Iqbal et al. [27], which is remarkably similar to our observations as shown in Fig. 5a.

4. Conclusions

By performing a systematic parametric study, we have elucidated the roles of the various ESEM processing parameters, namely, electron dose, acceleration voltage, chamber pressure, and dwell time, on the pattern resolution, strain and doping in graphene on SiO_2 substrates. Our experiments show that the highest pattern resolution is achieved with the lowest pressure and dwell times. In terms of controlling the extent of functionalization, as measured by the I_D/I_G values, we found that the electron dose was the single most important factor. Since the dose depends on both dwell time, beam current and pitch, and since we wish to keep dwell times short, regulating the pitch is therefore the best way to increase or decrease the electron dose. A correlation analysis between the G and 2D peak frequencies revealed a threshold dose above (below) which I_D/I_G was dominated by doping (strain). By comparing CVD-grown graphene with mechanically exfoliated graphene, we showed that this trend is universal, but the threshold values may vary due to differences in their initial defect densities. Future work will involve improving the pattern resolution down to the few-nm level, as well as studies on gases other than water vapor. Through our systematic studies, we uncovered the effects of the various ESEM parameters and show how defects can be engineered with great precision in graphene, thereby expanding the range of next-generation applications with respect to sensing and optoelectronics.

CRediT authorship contribution statement

Ryan Selhorst: Investigation, Writing – review & editing. **Michael A. Susner:** Conceptualization, Investigation, Writing – original draft. **Ryan Muzzio:** Investigation. **I-Hsuan Kao:** Investigation. **Jennifer Carpena-Núñez:** Investigation. **Ahmad E. Islam:** Investigation. **Jyoti Katoch:** Investigation. **Benji Maruyama:** Project administration. **Rahul Rao:** Conceptualization, Project administration, Supervision, Writing – original draft.

Declaration of competing interest

The authors declare the following financial interests/personal relationships which may be considered as potential competing interests: Rahul Rao reports financial support was provided by Air Force Office of Scientific Research.

Data availability

Data will be made available on request.

Acknowledgements

R.S., J.C–N., A.E.I., B.M., M.A.S., and R.R. acknowledge funding from the Air Force Office of Scientific Research under grant number 19RTXCOR052. J.K., I. K. and R.M. acknowledge funding provided by the Center for Emergent Materials at The Ohio State University, a National Science Foundation (NSF) MRSEC through Award No. DMR2011876. R.M. also acknowledges the NSF support through AGEP-GRS supplement to award DMR1809145.

Appendix A. Supplementary data

Supplementary data to this article can be found online at https://doi.org/10.1016/j.vacuum.2022.111686.

References

[1] F. Banhart, J. Kotakoski, A.V. Krasheninnikov, ACS Nano 5 (2011) 26–41.
[2] M. Batzill, Surf. Sci. Rep. 67 (2012) 83–115.
[3] S.-M. Lee, J.-H. Kim, J.-H. Ahn, Mater. Today 18 (2015) 336–344.
[4] H. Terrones, R. Lv, M. Terrones, M.S. Dresselhaus, Rep. Prog. Phys. 75 (2012), 062501.
[5] Y.-H. Zhang, Y.-B. Chen, K.-G. Zhou, C.-H. Liu, J. Zeng, H.-L. Zhang, Y. Peng, Nanotechnology 20 (2009), 185504.
[6] Z. Lin, B.R. Carvalho, E. Kahn, R. Lv, R. Rao, H. Terrones, M.E. Pimenta, M. Terrones, 2D Mater. 3 (2016), 022002.
[7] H. Yan, T. Low, W. Zhu, Y. Wu, M. Freitag, X. Li, F. Guinea, P. Avouris, F. Xia, Nat. Photonics 7 (2013) 394–399.
[8] X. Wang, Y. Ouyang, X. Li, H. Wang, J. Guo and H. Dai, Phys. Rev. Lett., , DOI: 10.1103/PhysRevLett.100.206803.
[9] B.S. Jessen, L. Gammelgaard, M.R. Thomsen, D.M.A. Mackenzie, J.D. Thomsen, J. M. Caridad, E. Duegaard, K. Watanabe, T. Taniguchi, T.J. Booth, T.G. Pedersen, A.-P. Jauho, P. Bøggild, Nat. Nanotechnol. 14 (2019) 340–346.
[10] K. Balasubramanian, T. Biswas, P. Ghosh, S. Suran, A. Mishra, R. Mishra, R. Sachan, M. Jain, M. Varma, R. Pratap and S. Raghavan, Nat. Commun., , DOI: 10.1038/s41467-019-09000-8.
[11] M.H. Rummeli, H.Q. Ta, R.G. Mendes, I.G. Gonzalez-Martinez, L. Zhao, J. Gao, L. Fu, T. Gemming, A. Bachmatiuk, Z. Liu, Adv. Mater. 31 (2019), 1800715.
[12] A. Chuvilin, J.C. Meyer, G. Algara-Siller, U. Kaiser, New J. Phys. 11 (2009), 083019.
[13] O. Dyck, S. Kim, E. Jimenez-Izal, A.N. Alexandrova, S.V. Kalinin, S. Jesse, Small 14 (2018), 1801771.
[14] O. Dyck, S. Kim, S.V. Kalinin, S. Jesse, Appl. Phys. Lett. 111 (2017), 113104.
[15] Ç.Ö. Girit, J.C. Meyer, R. Erni, M.D. Rossell, C. Kisielowski, L. Yang, C.-H. Park, M. F. Crommie, M.L. Cohen, S.G. Louie, A. Zettl, Science 323 (2009) 1705.
[16] D. Gunlycke, D.A. Areshkin, J. Li, J.W. Mintmire, C.T. White, Nano Lett. 7 (2007) 3608–3611.
[17] H.Q. Ta, A. Bachmatiuk, J.H. Warner, L. Zhao, Y. Sun, J. Zhao, T. Gemming, B. Trzebicka, Z. Liu, D. Pribat, M.H. Rümmeli, ACS Nano 10 (2016) 6323–6330.
[18] D.A. Areshkin, D. Gunlycke, C.T. White, Nano Lett. 7 (2007) 204–210.
[19] W.-K. Lee, K.E. Whitener, J.T. Robinson, P.E. Sheehan, Adv. Mater. 27 (2015) 1774–1778.

[20] F. Withers, T.H. Bointon, M. Dubois, S. Russo, M.F. Craciun, Nano Lett. 11 (2011) 3912–3916.
[21] B. Rajabifar, S. Kim, K. Slinker, G.J. Ehlert, A.J. Hart, M.R. Maschmann, Appl. Phys. Lett. 107 (2015), 143102.
[22] H. Miyazoe, I. Utke, J. Michler, K. Terashima, Appl. Phys. Lett. 92 (2008), 043124.
[23] D. Fox, A. O'Neill, D. Zhou, M. Boese, J.N. Coleman, H.Z. Zhang, Appl. Phys. Lett. 98 (2011), 243117.
[24] C. Thiele, A. Felten, T.J. Echtermeyer, A.C. Ferrari, C. Casiraghi, H.v. Löhneysen, R. Krupke, Carbon 64 (2013) 84–91.
[25] B. Song, G.F. Schneider, Q. Xu, G. Pandraud, C. Dekker, H. Zandbergen, Nano Lett. 11 (2011) 2247–2250.
[26] M.Z. Iqbal, S. Siddique, N. Anwar, Opt. Mater. 72 (2017) 496–500.
[27] M.W. Iqbal, A.K. Singh, M.Z. Iqbal, J. Eom 24 (2012), 335301.
[28] W. Shi, S. Kahn, L. Jiang, S.-Y. Wang, H.-Z. Tsai, D. Wong, T. Taniguchi, K. Watanabe, F. Wang, M.F. Crommie, Nat. Electron. 3 (2020) 99–105.
[29] Y. Zhou, J. Jadwiszczak, D. Keane, Y. Chen, D. Yu, H. Zhang, Nanoscale 9 (2017) 8657–8664.
[30] G. Liu, D. Teweldebrhan, A.A. Balandin, IEEE Trans. Nanotechnol. 10 (2010) 865–870.
[31] A.E. Islam, M.A. Susner, J. Carpena-Núñez, T.C. Back, R. Rao, J. Jiang, R. Pachter, S.A. Tenney, J.J. Boeckl, B. Maruyama, Carbon 166 (2020) 446–455.
[32] United States Provisional Patent, 62/405,657, .
[33] C.P. Royall, B.L. Thiel, A.M. Donald, J. Microsc. 204 (2001) 185–195.
[34] J.A. LaVerne, S.M. Pimblott, J. Phys. Chem. 95 (1991) 3196–3206.
[35] J. Carpena-Núñez, B. Davis, A.E. Islam, J. Brown, G. Sargent, N. Murphy, T. Back, M.R. Maschmann, B. Maruyama, Carbon 135 (2018) 270–277.
[36] A.C. Ferrari, Solid State Commun. 143 (2007) 47–57.
[37] M.A. Pimenta, G. Dresselhaus, M.S. Dresselhaus, L.G. Cançado, A. Jorio, R. Saito, Phys. Chem. Chem. Phys. 9 (2007) 1276–1290.
[38] A. Jorio, M.S. Dresselhaus, R. Saito, Raman Spectroscopy in Graphene Related Systems: Carbon Nanotubes, Nanographite and Graphene, Wiley-VCH, 2011.
[39] R. Rao, J. Reppert, X.F. Zhang, R. Podila, A.M. Rao, S. Talapatra, B. Maruyama, Carbon 49 (2011) 1318.
[40] A.C. Ferrari, J. Robertson, Phys. Rev. B 61 (2000) 14095–14107.
[41] A.C. Ferrari, J. Robertson, Phys. Rev. B 64 (2001), 075414.
[42] J. Jiang, R. Pachter, R.C. Selhorst, M.A. Susner, B. Maruyama, R. Rao, Appl. Surf. Sci. 589 (2022), 152953.
[43] A. Eckmann, A. Felten, A. Mishchenko, L. Britnell, R. Krupke, K.S. Novoselov, C. Casiraghi, Nano Lett. 12 (2012) 3925–3930.
[44] D.E. Newbury, J. Res. Natl. Inst. Stand. Technol. 107 (2002) 567.
[45] A. Das, S. Pisana, B. Chakraborty, S. Piscanec, S.K. Saha, U.V. Waghmare, K. S. Novoselov, H.R. Krishnamurthy, A.K. Geim, A.C. Ferrari, A.K. Sood, Nat. Nanotechnol. 3 (2008) 210–215.
[46] M. Huang, H. Yan, C. Chen, D. Song, T.F. Heinz, J. Hone, Proc. Natl. Acad. Sci. U.S. A. 106 (2009) 7304–7308.
[47] J. Jiang, R. Pachter, F. Mehmood, A.E. Islam, B. Maruyama, J.J. Boeckl, Carbon 90 (2015) 53–62.
[48] W.G. Burns, H.E. Sims, J. Chem. Soc. Faraday Trans. 1 Phys. Chem. Condens. Phases 77 (1981) 2803–2813.
[49] R. Rao, A. E. Islam, S. Singh, R. Berry, R. K. Kawakami, B. Maruyama and J. Katoch, Phys. Rev. B, , DOI:10.1103/PhysRevB.99.195401.
[50] J. E. Lee, G. Ahn, J. Shim, Y. S. Lee and S. Ryu, Nat. Commun., , DOI:10.1038/ncomms2022.
[51] Z. Wu, X. Zhang, A. Das, J. Liu, Z. Zou, Z. Zhang, Y. Xia, P. Zhao, H. Wang, RSC Adv. 9 (2019) 41447–41452.
[52] E. Koo, S.-Y. Ju, Carbon 86 (2015) 318–324.
[53] S. Ryu, L. Liu, S. Berciaud, Y.-J. Yu, H. Liu, P. Kim, G.W. Flynn, L.E. Brus, Nano Lett. 10 (2010) 4944–4951.
[54] J. Liu, Q. Li, Y. Zou, Q. Qian, Y. Jin, G. Li, K. Jiang, S. Fan, Nano Lett. 13 (2013) 6170–6175.
[55] E. Barros, K. Sato, G.G. Samsonidze, A. Souza Filho, M. Dresselhaus, R. Saito, Phys. Rev. B 83 (2011), 245435.
[56] S. Pisana, M. Lazzeri, C. Casiraghi, K.S. Novoselov, A.K. Geim, A.C. Ferrari, F. Mauri, Nat. Mater. 6 (2007) 198–201.
[57] P.R. Whelan, Q. Shen, B. Zhou, I.G. Serrano, M.V. Kamalakar, D.M.A. Mackenzie, J. Ji, D. Huang, H. Shi, D. Luo, M. Wang, R.S. Ruoff, A.-P. Jauho, P.U. Jepsen, P. Bøggild, J.M. Caridad, 2D Mater. 7 (2020), 035009.
[58] C. Hwang, D.A. Siegel, S.-K. Mo, W. Regan, A. Ismach, Y. Zhang, A. Zettl, A. Lanzara, Sci. Rep. 2 (2012) 590.
[59] R. Fates, H. Bouridah, J.-P. Raskin, Carbon 149 (2019) 390–399.